Journal of Hazardous Materials 390 (2020) 122165

Contents lists available at ScienceDirect

Journal of Hazardous Materials

journal homepage: www.elsevier.com/locate/jhazmat

Electrochemical adsorption of cadmium and arsenic by natural Fe-Mn nodules

Qi Qiao[a], Xiong Yang[a], Lihu Liu[a], Yao Luo[a], Wenfeng Tan[a], Chengshuai Liu[b], Zhi Dang[c], Guohong Qiu[a,*]

[a] Key Laboratory of Arable Land Conservation (Middle and Lower Reaches of Yangtse River), Ministry of Agriculture and Rural Affairs, Hubei Key Laboratory of Soil Environment and Pollution Remediation, College of Resources and Environment, Huazhong Agricultural University, Wuhan, 430070, Hubei Province, China
[b] State Key Laboratory of Environmental Geochemistry, Institute of Geochemistry, Chinese Academy of Sciences, Guiyang, 550081, China
[c] School of Environment and Energy, South China University of Technology, Guangzhou, 510006, China

GRAPHICAL ABSTRACT

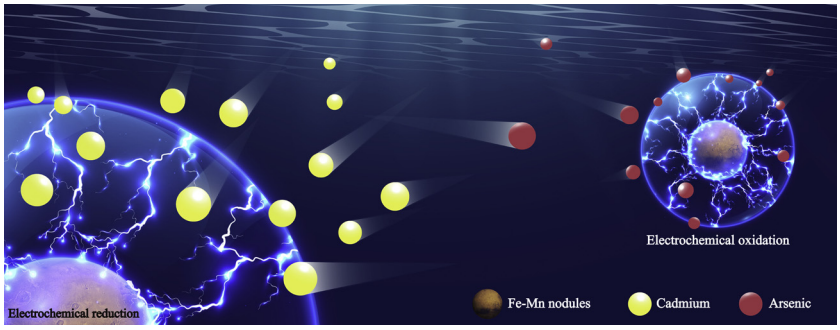

ARTICLE INFO

Editor: Xiaohong Guan

Keywords:
Fe-Mn nodule
Electrochemical adsorption
Cadmium
Arsenic
Redox

ABSTRACT

Fe-Mn nodules are widely distributed and regarded as excellent adsorbents for heavy metals. Their adsorption-desorption reactions with heavy metal ions are usually accompanied by redox processes. Herein, Fe-Mn nodules were used as adsorbents for Cd(II) and As(III,V) at a constant cell voltage under electrochemically controlled reduction and oxidation, respectively. The results showed that the adsorption performance for Cd(II) and As(III,V) was enhanced respectively due to the decrease and increase of Mn average oxidation state (Mn AOS) in Fe-Mn nodules. High birnessite content and Mn average oxidation state (Mn AOS) improved the adsorption of Cd(II) and As(III,V). The adsorption capacity for Cd(II) and total As increased with increasing voltage. With increasing pH, the adsorption capacity for Cd(II) increased first and then reached equilibrium, and that of total As decreased and then increased. The Cd(II) electrochemical adsorption capacity (129.9 mg g^{-1}) and the removal efficiency for total As at 1.2 V (83.6 %) in As-containing wastewater at an initial concentration of 4.068 mg L^{-1} were remarkably higher than the corresponding inorganic adsorption performance (9.46 mg g^{-1} and 70.5 %, respectively). This work may further promote the application of natural Fe-Mn nodules in the adsorption of heavy metals from wastewaters.

* Corresponding author.
E-mail address: qiugh@mail.hzau.edu.cn (G. Qiu).

https://doi.org/10.1016/j.jhazmat.2020.122165
Received 19 November 2019; Received in revised form 17 January 2020; Accepted 21 January 2020
Available online 22 January 2020

1. Introduction

Fe-Mn nodules, which are widely distributed in supergene soils and sediments, usually contain primary minerals such as quartz, feldspar and mica, and secondary minerals such as clay minerals and Fe and Mn oxides (Gasparatos, 2013). As the two most important components with high surface activities in Fe-Mn nodules, Mn oxides are excellent adsorbents for heavy metal cations due to their low point of zero charge (PZC) and high adsorption activity; and Fe (hydr)oxides have good affinity with heavy metal anions because of their large specific surface area and abundant hydroxyl groups (Feng et al., 2007; Gadde and Laitinen, 1974; Tan et al., 2005; Xu et al., 2012). Therefore, Fe-Mn nodules are widely used as adsorbents for heavy metal ions (Chakravarty et al., 2002; Deschamps et al., 2005; Maity et al., 2005; Tan et al., 2005).

The adsorption of heavy metals on Fe and Mn oxides usually involves different redox or complex reactions. For example, the adsorption of Sb(III) on birnessite includes a three-stage process of adsorption, desorption and re-adsorption of Sb, corresponding to the reduction, destruction of birnessite and then transformation into vernadite, respectively (Lu et al., 2019). Layer-structured birnessite has higher adsorption capacity for Cd(II) than tunnel-structured pyrolusite, cryptomelane and todorokite because of the additional adsorption of Cd(II) above/below the Mn(IV) vacancy sites at interlayers of birnessite in the form of triple-corner-sharing (TCS) complexes (Liu et al., 2019a; Peng et al., 2016; Wang et al., 2012). When being adsorbed by magnetite, Cr (VI) is reduced by the Fe(II) on the surface, followed by the formation of inner-sphere complex between Cr(III) and hydroxy groups (Yang et al., 2019b). During the oxidation of As(III) by birnessite, the presence of Fe (II) reduces the As(III) oxidation due to the competitive effect, and As prefers to bind with the newly formed Fe(III)-(hydr)oxides as a bidentate binuclear corner-sharing complex (Wu et al., 2018). As for the hydrogenetic ferromanganese nodules including vernadite (δ-MnO_2) and ferrihydrite, As and Mo are mainly adsorbed on ferrihydrite *via* double corner-shared (DCS) complexation and δ-MnO_2 *via* edge-shared (ES) complexation, respectively (Yang et al., 2019a).

Fe-Mn nodules from different soil environments show significant differences in their chemical composition, especially in the content and chemical valence state of Fe and Mn and crystal structures of Fe and Mn oxides, which result in different adsorption reactions and capacities for heavy metals. Five typical Fe-Mn nodules in Chinese soils vary greatly in the crystal structure of Mn and Fe oxides, the Fe and Mn contents (73.2–189.6 and 54.0–176.2 g kg^{-1}, respectively), and the corresponding Mn AOS (3.41–3.85) (Tan et al., 2005). In Fe-Mn nodules, the Fe and Mn contents affect the adsorption and enrichment for heavy metals. As reported, the enrichment capacity for Cd, Pb, Zn and Cu is related to the Mn content, and that for Cr is affected by the Fe content in nine typical Fe-Mn nodules of Chinese soils (Tan et al., 2006). The adsorption capacity of Fe and Mn oxides for heavy metals is largely determined by their crystal structure and chemical composition. As reported, the adsorption capacity of Mn oxides for Pb(II), Zn(II) and Cd (II) follows the order of birnessite > cryptomelane > todorokite > hausmannite (Feng et al., 2007). Due to its higher Mn AOS, birnessite generally contains more octahedral vacancies, which contribute to its higher adsorption capacity for Cd(II), Cu(II), Pb(II) and Zn(II) (Wang et al., 2012). The adsorption capacity of goethite (α-FeOOH) for As(III) is nearly two folds that of magnetite (Fe_3O_4), and that of hematite (α-Fe_2O_3) for As(V) is approximately three folds that of magnetite (Giménez et al., 2007). Therefore, adjustment of the chemical composition in Fe-Mn nodules may be an effective way to improve their adsorption capacity for heavy metals.

The redox reactions of Fe and Mn oxides often occur with changes in their chemical composition and adsorption capacity for heavy metal ions (Liu et al., 2017a; Peng et al., 2016; Yang et al., 2018). The adsorption for heavy metal cations can be facilitated by reduction reactions of Fe and Mn oxides. For example, the adsorption capacities of birnessite for Ni(II) and Zn(II) can be enhanced by the reduction transformation from birnessite to feitknechtite (β-MnOOH) and spinel $Zn(II)_{1-x}Mn(II)_xMn(III)_2O_4$ precipitates, respectively (Lefkowitz and Elzinga, 2015, 2017). The oxidation reaction promotes the adsorption of anions on Fe and Mn oxides (compounds). The arsenic adsorption capacity of siderite ($FeCO_3$) under oxic conditions is nearly 10 folds higher than that under anoxic conditions due to the oxidation transformation from siderite to goethite (Guo et al., 2013). Therefore, the regulation of redox reactions is a promising method to change the chemical composition of Fe and Mn oxides and improve their adsorption performance.

Electrochemical techniques can be used to effectively control the redox reaction degree and the corresponding chemical composition of Fe and Mn oxides, which may significantly improve the adsorption capacity for heavy metals. Our previous study has indicated that when redox reactions are controlled by galvanostatic charge-discharge, the Mn AOS and the surface adsorption sites of birnessite decrease and increase, respectively, with the maximum adsorption capacity for Cd (II), Cu(II) and Zn(II) reaching 900.7, 372.3 and 530.0 mg g^{-1}, which are nearly 6, 7 and 8 folds higher than the corresponding isothermal adsorption capacity (Liu et al., 2017a; Peng et al., 2016; Yang et al., 2018). The electrochemical adsorption capacity for Ni(II) by α-MnO_2/carbon fiber paper can reach 16.4 mg g^{-1}, which is significantly higher than that of single carbon fiber paper (0.034 mg g^{-1}), because of the presence of Mn oxide and changes in its chemical composition including the decrease in Mn AOS (Li et al., 2018). Therefore, electrochemical redox reactions can promote the adsorption performance of Fe and Mn oxides for heavy metals.

Natural Fe-Mn nodules are widely distributed in nature and can be easily collected at low cost (Liu et al., 2002), exhibiting great potential to be applied to real wastewater treatment. However, the electrochemical adsorption mechanism of the natural Fe-Mn nodules containing Fe and Mn oxides with different crystal structures may be more complicated than that of synthesized iron and manganese oxides. In addition, the chemical composition of natural Fe-Mn nodules varies with regions, which may have a significant effect on their electrochemical adsorption performance. In this work, typical Fe-Mn nodules in China were collected and used to electrochemically adsorb and remove cadmium and arsenic from wastewaters. The adsorption mechanism was studied, and the key chemical component in Fe-Mn nodules influencing the electrochemical adsorption for Cd(II) and As (III,V) was investigated, which is of great significance for the selective exploitation and application of natural minerals.

2. Materials and methods

2.1. Sample preparation

Fe-Mn nodules were collected from three typical regions of China, Tai'an city (37°33′27″N, 116°59′55″E), Linyi city (34°22′46.5″N, 117°37′5″E) in Shangdong province, and Zaoyang city (32°16′55.7″N, 112°31′38.5″E) in Hubei province, which were named as TA, LY and ZY, respectively. The collected nodule samples were washed three times by deionized water and then one time by ethanol. The cleaned nodules were dried in a vacuum oven at 40 °C for 12 h, and then ground and sieved with 100 mesh sieves. The photos of TA, LY and ZY, and the corresponding powder microstructures are shown in Fig. S1. Other chemical composition of the nodules, including the contents of some metal elements, particle distribution and clay mineral composition (Fig. S2), is described in Table S1. The detailed preparation process of Fe-Mn nodule electrodes is shown in Supporting Information.

2.2. Electrochemical adsorption of Cd(II)

Electrochemical adsorption of Cd(II) was carried out in a 100 mg L^{-1} Cd(II) solution at initial pH 5.0 with 0.1 mol L^{-1} Na_2SO_4 as the

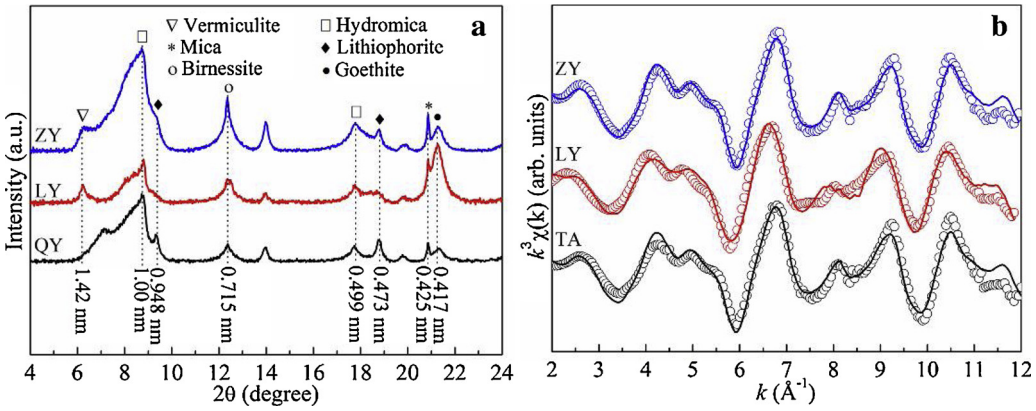

Fig. 1. XRD patterns (a) of TA, LY and ZY clay fractions treated by NaOH and Mn K-edge k^3-weighted EXAFS (b) of TA, LY and ZY clay fractions (the open circles are experimental curves and the lines are the best-fit linear combinations).

background electrolyte. It was performed in a two-electrode system involving 30 mL of wastewater, in which the electrode containing 10 mg of Fe-Mn nodules was used as the cathode (2.5 cm × 3.5 cm) and a blank graphite paper was used as the anode (2.5 cm × 3.5 cm) at 0–0.9 V for 12 h. The effect of pH on the electrochemical adsorption capacity for Cd(II) was investigated using ZY in 100 mg L^{-1} Cd(II) solution with initial pH 3.0–6.0. To investigate the effect of chemical composition on adsorption capacity, the three types of Fe-Mn nodules were used to electrochemically adsorb Cd(II) in 100–1200 mg L^{-1} Cd(II) solution. Cyclic voltammetry test was conducted on the electrochemical workstation (CHI660E, Shanghai Chenhua Instrument Co. Ltd., China) to study the electrochemical adsorption behavior of Cd(II) on the surface of Fe-Mn nodules within a potential window of 0–0.9 V (*vs.* SCE) at a scan rate of 0.5 mV s^{-1}. The isothermal adsorption of Cd(II) on the Fe-Mn nodules was also conducted for the comparation with the electrochemical adsorption, and the details are provided in Supporting Information.

2.3. Adsorption of As(III,V) from industrial wastewater

The As-containing wastewater was collected from a ditch (30°10′18″N, 114°55′47″E) near a factory in Daye city of Hubei province and filtered with 0.45 μm filter membrane. The concentrations of total As, As(III) and Mn(II) in wastewater were 4.068, 0.459 and 4.90 mg L^{-1}, respectively, with pH 7.8. In 30 mL of wastewater, a two-electrode system including an anode containing 70 mg of Fe-Mn nodules (6.5 cm × 7.9 cm) and a blank graphite paper cathode (6.5 cm × 7.9 cm) was used to electrochemically adsorb As at 0.3–1.2 V for 12 h. The total As removal efficiency of Fe-Mn nodules was also evaluated at open circuit for comparison. The concentrations of anion Cl–, NO_3– and SO_4^{2-} were 62.70, 32.66 and 1043.52 mg L^{-1}, respectively, in the As-containing wastewater. The effect of pH on the electrochemical adsorption of As was studied with initial pH 5.0–7.8 adjusted by 0.1 mol L^{-1} H_2SO_4. The three types of Fe-Mn nodules were used to electrochemically adsorb As in As-containing wastewater to investigate the influence of chemical composition on their adsorption performance. All electrochemical adsorption experiments were carried out for three times on the battery test system (Shenzhen Neware Electronic Ltd., China).

2.4. Chemical analysis and characterization

Particle distribution of the three types of Fe-Mn nodules was determined by the pipette-extraction method (Robinson, 1922). The clay fractions of Fe-Mn nodules were separated by siphon according to Stoke's Law (Singh et al., 2016). The relative contents of phyllosilicates were determined by X-ray diffraction (XRD, Bruker D8 Advance diffractometer with Cu Kα, a tube voltage of 40 kV, a tube current of 40 mA, and a step interval of 0.02°) semi-quantitative analysis (Pai et al., 1999; Srodon, 2006). The crystal structure types of Fe and Mn oxides were determined by XRD after treatment of the clay fractions with NaOH solution (Tokashiki et al., 2003). A Zetasizer 3600 (Malvern Instrument, USA) was used to determine the zeta potential values of the samples in 1.0 mmol L^{-1} KNO_3. Atomic absorption spectroscopy (AAS, Varina AAS240FS) was used to analyze the contents of some metallic elements in Fe-Mn nodules after microwave digestion (Sandroni et al., 2003). XAFS spectra were collected on the 1W1B beamline at Beijing Synchrotron Radiation Facility of China to analyze the relative contents of different types of Mn oxides and Mn AOS, and the detailed parameters of spectra analysis are shown in Supporting Information.

Before and after adsorption reactions, the chemical composition and micromorphology of Fe-Mn nodules were respectively characterized by Fourier transform infrared spectrometer (FTIR, Bruker VERTEX 70) and FESEM (Hitachi, SU8000). The relative contents and distribution of elements on nodule surface were determined by energy dispersive spectrum (EDS). The relative contents and valence states of elements on the nodule surface were analyzed by X-ray photoelectron spectroscopy (XPS, Multilab 2000) with Mg Kα at 1253.6 eV, using C 1s peak (284.6 eV) as charge reference. The concentrations of Cd, Fe, Mn, Cr, Cu, Pb, Zn, Co and Ni in the solutions were determined by AAS, and those of Cl^-, NO_3^- and SO_4^{2-} were determined by an ion chromatograph (Dionex ICS-1100). The concentration of total As and As(III) in the liquid phase was quantified by an atomic fluorescence spectrometer (AFS9700, Beijing Haiguang Instrument Co. Ltd.) using 5 % HCl − 2 % KBH_4 solution and 1.5 % HCl − 1.5 % KBH_4 solution as the carrying fluid, respectively (Xu et al., 2013).

3. Results

3.1. Characterization of chemical composition of Fe-Mn nodules

As indicated by the XRD patterns and FTIR spectra (Figs. 1a and S3), goethite, birnessite and lithiophorite were the main Fe and Mn oxides in TA, LY and ZY. The contents of MnO_2 and FeOOH, which represent Mn and Fe oxides, were 95.7 and 196.3 g kg^{-1} in TA, 114.3 and 341.0 g kg^{-1} in LY, and 93.6 and 229.0 g kg^{-1} in ZY, respectively (Table S1). The Mn extended X-ray absorption fine-structure (EXAFS) spectra indicated that among the Mn oxides, birnessite and lithiophorite showed relative contents of 90.3 % and 9.7 % in TA, 51.0 % and 49.0 % in LY, and 97.3 % and 2.7 % in ZY, respectively (Fig. 1b and Table S2). Furthermore, the mass contents of birnessite, lithiophorite and goethite were 86.4, 9.3 and 196.3 g kg^{-1} in TA, 58.3, 56.0 and 341.0 g kg^{-1} in LY, and 91.1, 2.5 and 229.0 g kg^{-1} in ZY, respectively. The Mn AOS in TA, LY and ZY was measured to be 3.19, 3.61 and 3.40, respectively

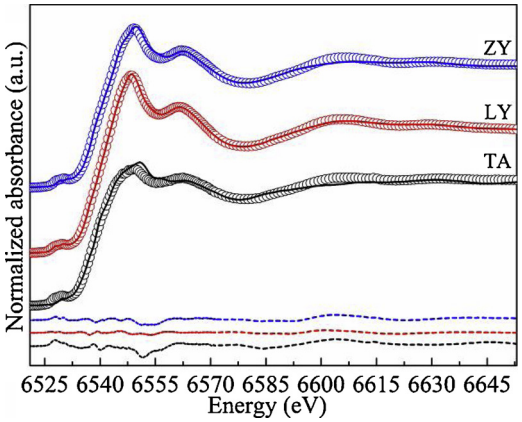

Fig. 2. Normalized Mn K-edge XANES spectra and best-fitted curves (lines) of TA, LY and ZY clay fractions using the Combo method (difference plots are indicated at the bottom).

(Fig. 2 and Table S3).

3.2. Electrochemical adsorption of Cd(II) on Fe-Mn nodules

The electrochemical adsorption behavior of Cd(II) on the surface of Fe-Mn nodules was investigated by cyclic voltammetry. Fig. S4a shows the cyclic voltammetry curve of ZY electrode in Cd(II) solutions at different concentrations. A pair of redox current peaks were observed on the cyclic voltammetry curve for the solution of 1200 mg L^{-1} Cd(II). The reduction and oxidation current peaks at about 0.2 V and 0.45 V represented the reduction of Mn(IV) to Mn(III) with the intercalation of Cd(II) into ZY surface, and the oxidation of Mn(III) to Mn(IV) with the deintercalation of Cd(II) from ZY surface, respectively (Peng et al., 2016). With increasing Cd(II) concentration, the CV curve gradually increased in intensity and deviated from the rectangle shape, suggesting an increase in specific capacity but a decrease in reversibility due to the intercalation of Cd(II). Compared with ZY, LY had lower redox current and a slighter deviation from the rectangle shape, indicating its lower specific capacity and the redox activity (Fig. S4b).

The adsorption of Cd(II) on Fe-Mn nodules under electrochemical reduction was investigated in a two-electrode system with Fe-Mn nodules as the cathode and a graphite paper as the anode at 0.9 V in 100 mg L^{-1} Cd(II) solution. The electrochemical adsorption capacity of ZY for Cd(II) gradually increased with time and reached equilibrium at 12 h (Fig. 3a). The influence of voltage on the adsorption capacity was studied using ZY for 12 h within the range of 0–0.9 V. The results showed that with increasing voltage, the potential of ZY electrode decreased (Fig. S5), and the adsorption capacity increased and reached a maximum of 43.6 mg g^{-1} at 0.9 V (Fig. 3b). The effect of pH on the electrochemical adsorption capacity for Cd(II) was investigated using ZY in 100 mg L^{-1} Cd(II) solution with initial pH 3.0–6.0. After electrochemical adsorption, the pH of the solution increased to 3.19 ± 0.02, 4.70 ± 0.20, 5.86 ± 0.45 and 6.00 ± 0.13 when the initial pH was controlled at 3.0, 4.0, 5.0 and 6.0, respectively. The adsorption capacity for Cd(II) and the released Mn(II) respectively increased and decreased, and then reached equilibrium at initial pH 5.0 (Figs. 3c and S6). The release ratio of Fe was 3.0 % with initial pH 3.0, and dissolved Fe could not be detected when the pH was increased to above 4.0. After electrochemical adsorption, the ZY sample was further characterized by XRD, and no significant change was observed in mineral crystal structure (Fig. S7).

Fig. 4a displays the adsorption capacities of three types of Fe-Mn nodules in 0–1200 mg L^{-1} Cd(II) solution for 12 h at 0.9 V. The electrochemical adsorption capacity for Cd(II) generally increased with increasing initial Cd(II) concentration for all types of Fe-Mn nodules, and the highest adsorption capacity of TA, LY and ZY was 51.8, 113.1 and 129.9 mg g^{-1}, respectively. The currents in the reaction systems with different Fe-Mn nodules in 1200 mg L^{-1} Cd(II) solution at 0.9 V followed the order of ZY > LY > TA (Fig. S8), which was consistent with the order of electrochemical adsorption capacity for Cd(II). Increases in initial Cd(II) concentration resulted in higher Mn^{2+} release ratios, and the maximum release ratio of Mn from ZY, LY and TA was 14.1 %, 7.4 % and 3.7 %, respectively (Fig. S9a), which was consistent with the order of response current.

The isothermal adsorption capacity was compared with the electrochemical adsorption capacity. The adsorption isotherm equation was fitted by the Langmuir model (Fig. 4b), and the isothermal adsorption capacities of TA, LY and ZY were 4.79, 5.73 and 9.46 mg g^{-1}, respectively, which were significantly lower than the corresponding electrochemical adsorption capacities. Increases in equilibrium Cd(II) concentration would result in increases in Mn^{2+} release ratio, and the maximum Mn release ratio from TA, ZY and LY was respectively 1.6 %, 1.5 % and 0.2 % (Fig. S9b), which had negative correlations with Mn AOS. The concentration of Fe-Mn nodules used in isothermal and electrochemical adsorption was 10 and 0.33 g L^{-1}, respectively. The concentrations of released Fe and heavy metal ions of Cr, Cu, Pb, Zn, Co, Ni and As from Fe-Mn nodules were below the detection limit after adsorption, indicating that the heavy metal ions released from the nodules would not cause secondary pollution to the environment.

To study the electrochemical adsorption mechanism, XRD and FTIR were used to characterize ZY electrode before and after adsorption at 0.9 V in solutions with different concentrations of Cd(II) (Fig. S10). The XRD characteristic diffraction peaks of ZY showed no obvious changes after adsorption, indicating that no new substances were formed. After adsorption, the diffraction peak at 0.715 nm attributed to the (001) crystal surface of birnessite increased, and the intensity of the characteristic absorption bands of birnessite at 497 and 451 cm^{-1} was also enhanced (Ling et al., 2017). As shown in Fig. 5, flower-like microspheres specific for birnessite were observed after adsorption, which further confirmed the results of XRD and FTIR. No significant difference was observed in the mineral crystal structures, characteristic functional groups and microstructures of TA and LY before and after electrochemical adsorption (Figs. S11–S13).

EDS was further used to investigate the changes in element composition and distribution on ZY surface after adsorption in 1200 mg L^{-1} Cd(II) solution at 0.9 V (Fig. 6). The element distribution on ZY surface before (Area 1, 2) and after adsorption (Area 3, 4) is shown in Fig. 6e–h. The relative contents of Mn, O and Cd on ZY surface increased and flower-like microspheres were formed after adsorption. In Area 1, 2 and 4, the relative contents of Mn were 2.1 %, 3.1 % and 31.3 %, those of O were 3.2 %, 5.2 % and 21.9 %, and those of Cd were 1.1 %, 1.0 % and 4.2 %, respectively (Table S4). The results further showed that the flower-like microspheres were birnessite with adsorption of Cd(II) on its surface.

Before and after electrochemical adsorption, the chemical composition of ZY surface was analyzed by XPS. The relative contents of Mn and O increased, which could be attributed to the exposure of birnessite from the inside of electrode due to the reduction dissolution of nodules on the basis of XRD and FTIR results (Fig. 7a and Table S5). The relative content of Cd also increased, indicating the adsorption of Cd (Fig. 7b). Peak fitting of Mn $2p_{3/2}$ was performed to analyze the valence state of Mn in the sample (Fig. 7c–d). After adsorption, the relative contents of Mn(II) and Mn(III) were elevated from 9.5%–19.1% and 40.2%–42.7%, respectively. The relative content of Mn(IV) and the corresponding Mn AOS dropped from 50.3%–38.3 % and 3.41 to 3.19, respectively, indicating the reduction of Mn oxides on ZY surface. The Fe on ZY surface existed in the form of Fe(III) without change in valence state, as indicated by the same peak position of 712.0 eV in Fe $2p_{3/2}$ spectrum before and after adsorption (Fig. S14) (Peng et al., 2017; Zhang et al., 2007).

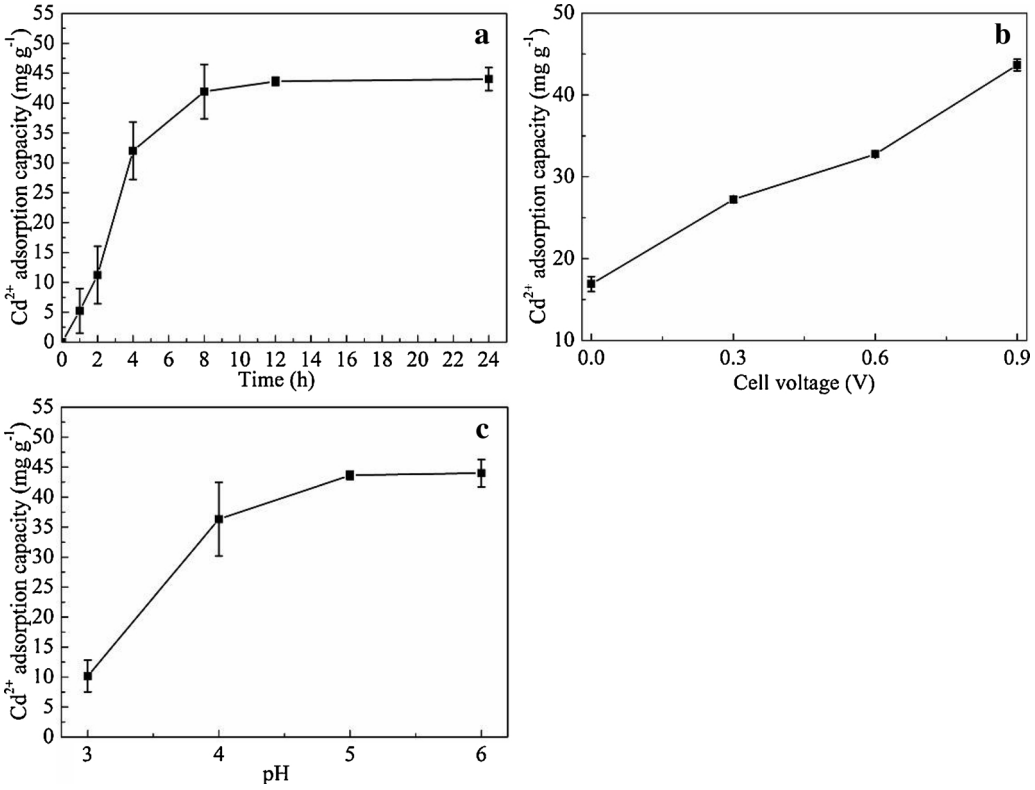

Fig. 3. Cd^{2+} electrochemical adsorption capacity of ZY in 100 mg L^{-1} Cd^{2+} solution with initial pH 5.0 at 0.9 V for 0–24 h (a) and at 0–0.9 V for 12 h (b), and with initial pH 3.0–6.0 at 0.9 V for 12 h (c).

3.3. Electrochemical adsorption of As on Fe-Mn nodules

To investigate the adsorption behavior of Fe-Mn nodules for heavy metal anions under electrochemical oxidation, As(III,V) in the wastewater was adsorbed at 1.2 V in a two-electrode system with ZY as the anode and a blank graphite paper as the cathode. The concentrations of total As, As(III) and Mn(II) gradually decreased from 4.068, 0.459 and 4.90 mg L^{-1} to 0.669, 0.088 and 0.19 mg L^{-1} after 12 h, respectively (Fig. 8a). The effect of voltage and corresponding potential on adsorption was further investigated with adsorption of 12 h. The potential of ZY anode increased with increasing voltage (Fig. S15a). The application of voltage and increases of voltage within 0.3–1.2 V greatly improved the electrochemical adsorption performance of ZY for As, and significantly decreased the Mn(II) concentration in wastewater (Fig. 8b). The effect of initial pH within the range of 5.0–7.8 on the electrochemical adsorption of As was investigated. With increasing pH, the potential of ZY electrode decreased (Fig. S15b), and the residual concentrations of total As, As(III) and Mn(II) in the solution increased first and then decreased after electrochemical adsorption for 12 h. The maximum residual concentration of total As and As(III) reached 0.956 and 0.119 mg L^{-1} at pH 7.0, respectively, and that of Mn(II) was 0.46 mg L^{-1} at pH 6.0 (Fig. 8c).

To study the effect of the chemical composition of Fe-Mn nodules on the adsorption for As, TA and LY were used as the anode instead of ZY, and blank carbon paper was used as the cathode to adsorb As(III,V) from wastewater at 1.2 V for 12 h. The concentration of total As decreased from 4.068 to 1.104 and 1.193 mg L^{-1}, and that of As(III) decreased from 0.459 to 0.183 and 0.146 mg L^{-1} after electrochemical adsorption by TA and LY, respectively. The removal efficiency of total As followed the order of ZY (83.6 %) > TA (72.9 %) > LY (70.7 %). The concentration of Fe-Mn nodules used in electrochemical adsorption was 2.33 g L^{-1}. The concentrations of released Fe and heavy metal ions of Cr, Cu, Pb, Zn, Co and Ni from Fe-Mn nodules were below the detection limit after adsorption, indicating that the heavy metal ions released

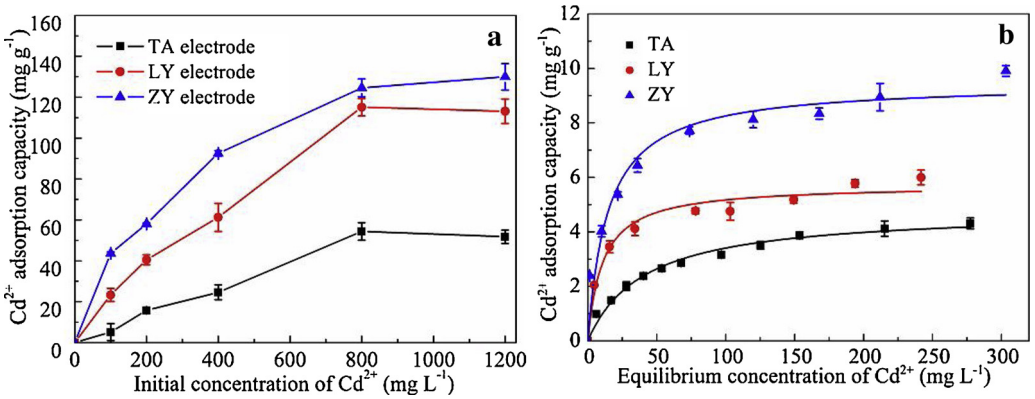

Fig. 4. Cd^{2+} electrochemical adsorption capacity of Fe-Mn nodules at 0.9 V for 12 h (a) and isothermal adsorption curves of Fe-Mn nodules with pH 5.0 at 25 °C (b).

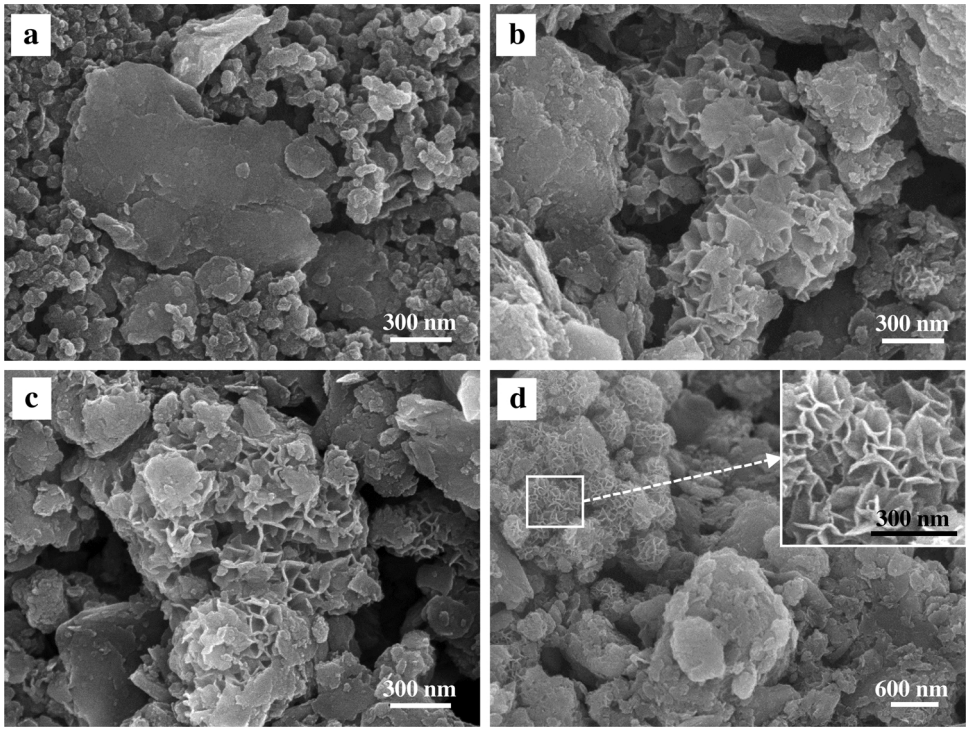

Fig. 5. FESEM images of ZY before (a) and after electrochemical adsorption at 0.9 V in Cd^{2+}-containing solutions with different concentrations: 100 mg L^{-1} (b), 400 mg L^{-1} (c) and 1200 mg L^{-1} (d).

from the nodules would not cause secondary pollution.

ZY was further characterized by XRD and XPS to analyze the electrochemical reaction mechanism. No significant change in mineral crystal structure of ZY was observed after adsorption (Fig. S16). As indicated by the XPS broad scans, the relative contents of Mn and O increased on the ZY surface after adsorption at 1.2 V in As-containing wastewater (Fig. 9a and Table S6), indicating the formation of Mn oxides. A new peak at 45.36 eV corresponding to As 3d was observed, indicating that As(V) was adsorbed on the anode surface (Fig. 9b) (Nesbitt et al., 1998; Peng et al., 2017). After adsorption, the relative contents of Mn(II) and Mn(III) decreased from 9.5%–6.5 % and 40.2%–21.1%, respectively. The relative content of Mn(IV) and the corresponding Mn AOS increased from 50.3%–72.4% and 3.41–3.66, respectively (Fig. 9c–d), and O in the state of O^{2-} increased from 3.9%–13.8% (Fig. S17a), further indicating that Mn oxides were formed on ZY surface after electrochemical oxidation of Mn(II/III). Fe existed in the form of Fe (III) on ZY surface without change in valence state, as indicated by the same peak position of 712.0 eV in Fe $2p_{3/2}$ spectrum before and after adsorption (Fig. S17b) (Peng et al., 2017; Zhang et al., 2007).

4. Discussion

4.1. Electrochemical adsorption mechanism for cadmium

The Cd(II) adsorption capacity of Fe-Mn nodules was compared with that of some natural adsorbents (Table S7). In this work, the Cd(II) isothermal adsorption capacities of the three types of Fe-Mn nodules were within 4.8–9.5 mg g^{-1}, which are close to those reported in literature (Table S7). The Cd(II) adsorption capacity of Fe-Mn nodules under electrochemical reduction was enhanced to 129.9 mg g^{-1}, which is significantly higher than that of some natural adsorbents, including kaolinite, vermiculite, montmorillonite and manganese nodule residue with the Cd(II) adsorption capacity of 6.8, 19.7, 30.7 and 42.5 mg g^{-1}, respectively. Reduction of transition metal oxides including MnO_2 is usually accompanied by the adsorption of cations such as Na^+, K^+ and H^+ (Zhang and Chen, 2008; Zhang et al., 2018). Hence, the reduction reactions of Mn oxides can be applied to seawater desalination (Lee et al., 2014b; Liu et al., 2016). Our previous work has shown that reduction reactions of Mn oxides can also be used to remove heavy metal cations (Liu et al., 2017a, 2017b; Peng et al., 2016; Yang et al., 2018). Fe and Mn oxides are abundant transition metal oxides in Fe-Mn nodules, and their reduction reactions may promote the adsorption for Cd (II). Thus, the adsorption capacity for Cd(II) under electrochemical reduction was significantly higher than that under isothermal adsorption (Fig. 4).

The changes in the chemical composition of Mn oxides under electrochemical reduction reactions may be favorable to Cd(II) adsorption. Mn AOS on the surface of nodules decreased after electrochemical adsorption (Fig. 7c–d). The electrochemical reduction from Mn(IV) to Mn(II/III) increased the negative charge on the surface, and then more Cd(II) was adsorbed on Mn oxide surface to balance the increased negative charge (Figs. 6 and 7b). Therefore, Mn oxides play a critical role in electrochemical adsorption. Our previous work has demonstrated that Zn(II) adsorption is promoted by the reduction transformation of birnessite to hetaerolite ($ZnMn_2O_4$) (Liu et al., 2017b).

The different reduction characteristics of Fe and Mn oxides at low potential indicate that the reduction of Mn oxides rather than iron oxides promotes the adsorption capacity for Cd(II). Reduction from Mn (IV) to Mn(III) is easier to occur than that from Fe(III) to Fe(II) at low potential, due to the higher redox potential of Mn(IV)/Mn(III) pair (Marcus et al., 2004). During the adsorption reaction, Mn(III) from reduced Mn(IV) is disproportionated by the Jahn-Teller effect (Lee et al., 2014a), resulting in the release of Mn(II) into the solution (Figs. 7c–d and S9a). However, the reduction and dissolution of Fe(III) was not observed. Fe(II) is easily oxidized to Fe(III) to form ferrihydrite nanoparticles once Fe(III) is reduced (Boland et al., 2014). Mineral-phase transformation of goethite was not observed, and dissolved Fe (II,III) was not detected in the liquid phase, indicating that the reduction dissolution of Fe(III) could be neglected during electrochemical adsorption (Fig. S10).

Multiple regression analysis showed that birnessite is the key

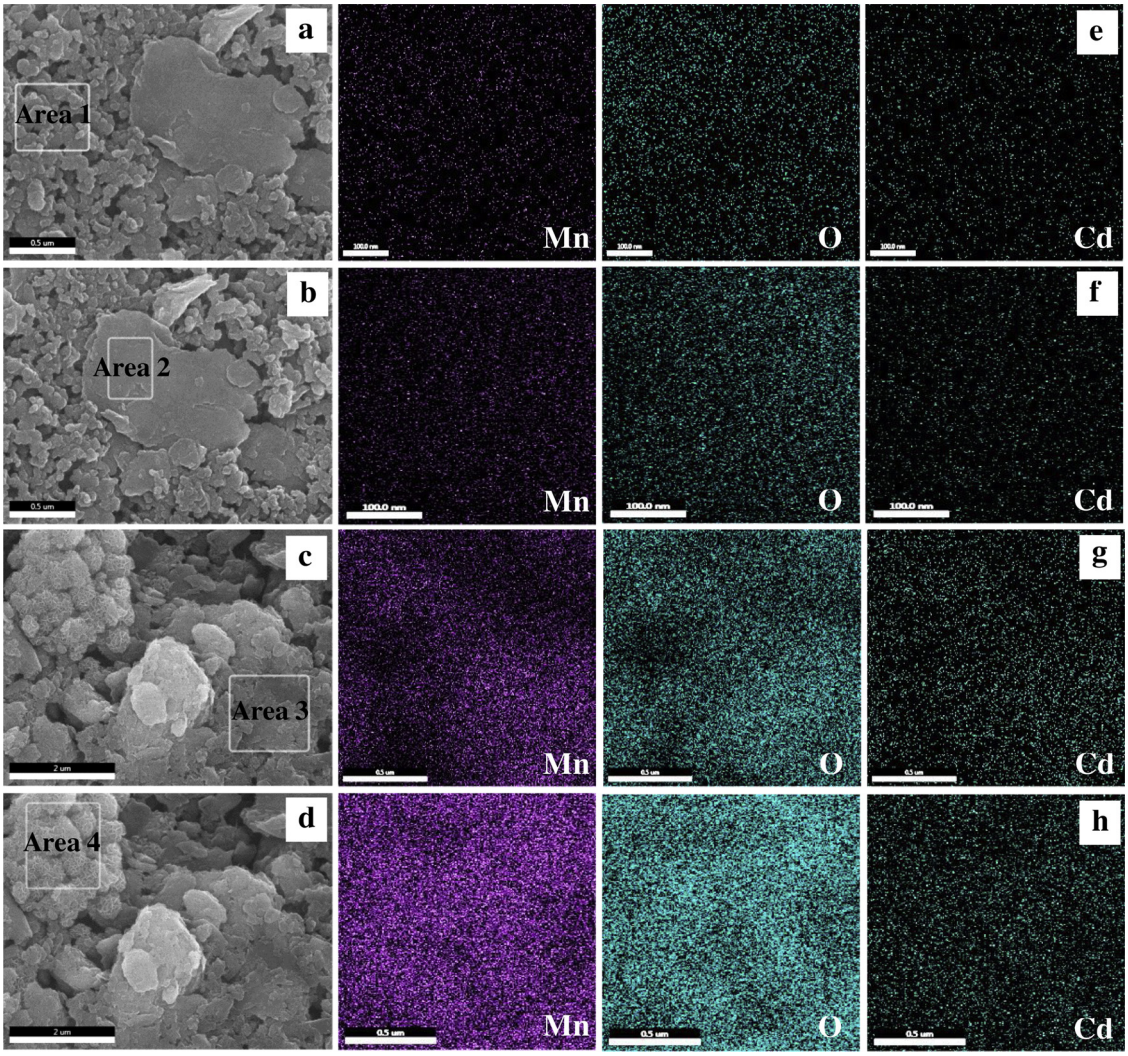

Fig. 6. FESEM images of ZY before (a, b) and after electrochemical adsorption at 0.9 V in 1200 mg L^{-1} Cd^{2+} solution (c, d), and EDX mappings of Mn, O and Cd in Area 1 (e), 2 (f), 3 (g) and 4 (h).

component for Cd(II) adsorption (Table S8) owing to its surface charge and crystal structure. The Cd(II) adsorption is facilitated by negative charge on the surface. The PZC of natural birnessite (2.8) is significantly lower than that of natural lithiophorite (6.9) and goethite (4.0–9.2) (Kim et al., 2002; Kosmulski, 2009). Cd(II) is adsorbed on Fe and Mn oxides mainly in the form of hydroxylation cations *via* hydrolysis induced by the more negative charge on mineral surfaces (Feng et al., 2007). The formation of hydroxylation cations decreases the hydration degree of Cd(II) as hydrated ions, and adsorption is thus improved due to the lowered energy barriers for specific adsorption (Feng et al., 2007). Also, the crystal structure of minerals significantly affects their adsorption capacity. As a layer-structured Mn oxide formed by the stacking of MnO_6 octahedron layers and water molecular layers, birnessite possesses many vacancies in the structure of MnO_6 octahedron layers, and the ratio of vacancies can reach 16.7 % (Lanson et al., 2000). The interlayer sites above and below vacancies are strong adsorption sites for heavy metals (Wang et al., 2012). However, as a layer-structured Mn oxide formed by the stacking of MnO_6 octahedron layers and $LiAl_2(OH)_6$ octahedron layers, lithiophorite does not contain vacancies in the structure of MnO_6 octahedron layers (Feng et al., 2004; Yang and Wang, 2003; Zhao et al., 2016). Goethite has a tunnel structure with the stacking of FeO_6 octahedrons, and Cd(II) is only adsorbed at the surface sites of goethite to form complexes rather than in the tunnel (Collins et al., 1999). The limited number of adsorption sites may lead to low adsorption capacity.

The cyclic voltammetry curves further revealed the electrochemical adsorption process of Cd(II) on birnessite. Our previous results have indicated that Cd(II) is usually adsorbed above/below the octahedral vacancies in the birnessite in the form of triple-corner-sharing (TCS) inner-sphere complexes (Wang et al., 2012). In this work, the cyclic voltammetry curve of ZY also indicated the formation of inner sphere complexes between Cd(II) and birnessite due to the redox reactions (Fig. S4a). The cyclic voltammetry curve gradually deviated from the rectangle with increasing Cd(II) concentration. The obvious reduction and oxidation current peaks appeared at around 0.2 and 0.45 V, respectively, which represent the intercalation and incomplete reversible deintercalation of Cd(II) on the surface of birnessite. This irreversible intercalation − deintercalation reaction is likely due to the formation of inner-sphere complex. No obvious redox current peak was observed in the cyclic voltammetry curve of LY possibly due to the low content of birnessite (Fig. S4b).

Mn AOS directly reflects the chemical composition and redox behavior of Fe-Mn nodules, and also affects the electrochemical adsorption capacity for Cd(II). The presence of adsorbed Mn(II) decreased the Mn AOS of Mn oxides with a corresponding decrease in Cd(II) electrochemical adsorption capacity of the Fe-Mn nodules in this work. That is to say, high Mn AOS contributes to higher adsorption activity of Mn oxides. Multiple regression analysis also proved that high Mn AOS

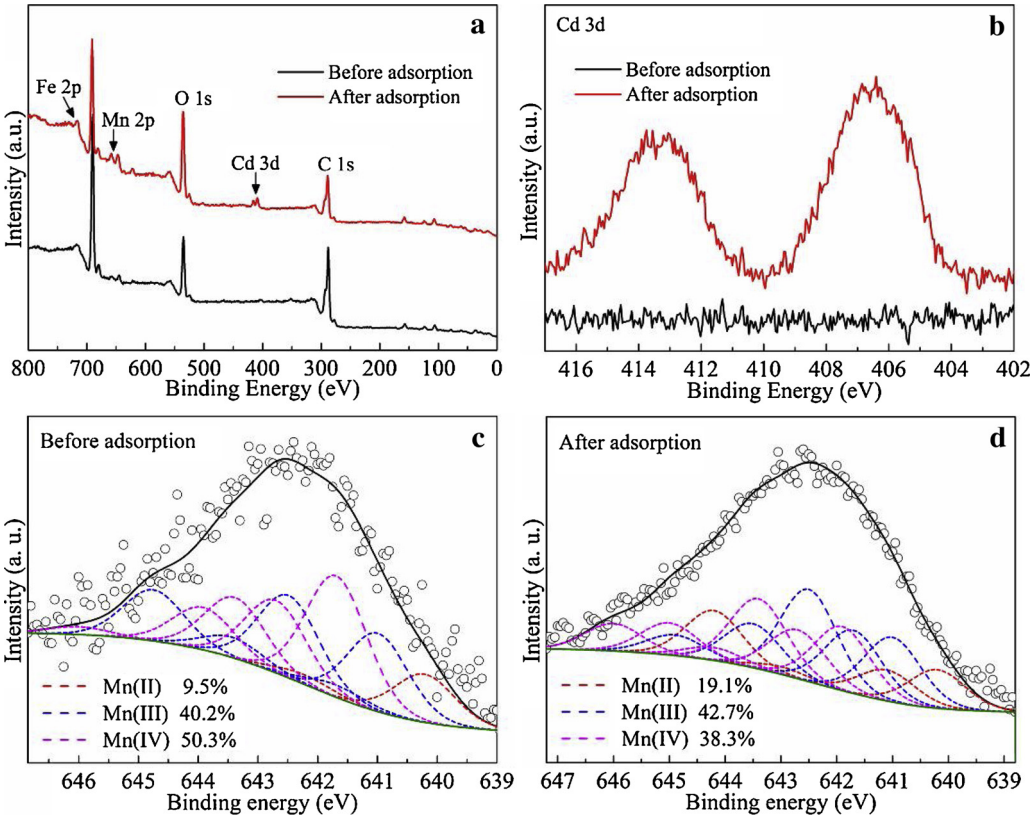

Fig. 7. XPS broad scans (a), Cd 3d (b) and Mn $2p_{3/2}$ (c, d) of ZY before and after electrochemical adsorption at 0.9 V in 1200 mg L^{-1} Cd^{2+} solution.

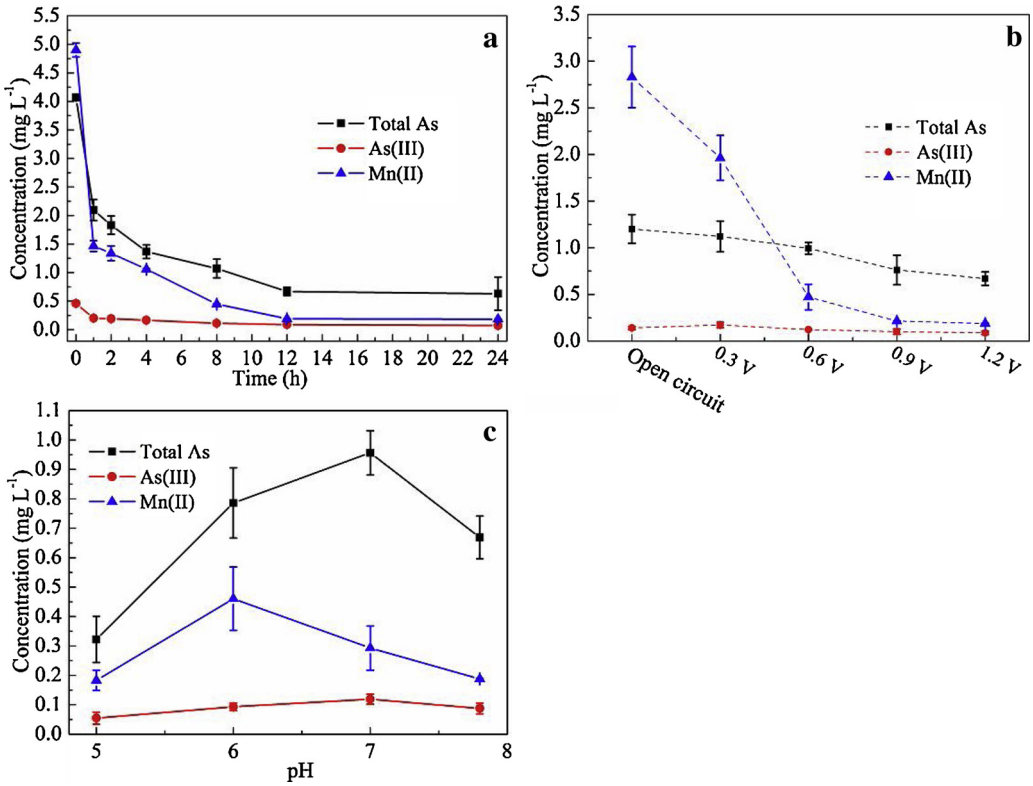

Fig. 8. As and Mn(II) concentration after electrochemical adsorption by ZY in wastewaters with initial pH 7.8 at 1.2 V for 0–24 h (a) and at open circuit and 0.3–1.2 V for 12 h (b), and with initial pH 5.0–7.8 at 1.2 V for 12 h (c).

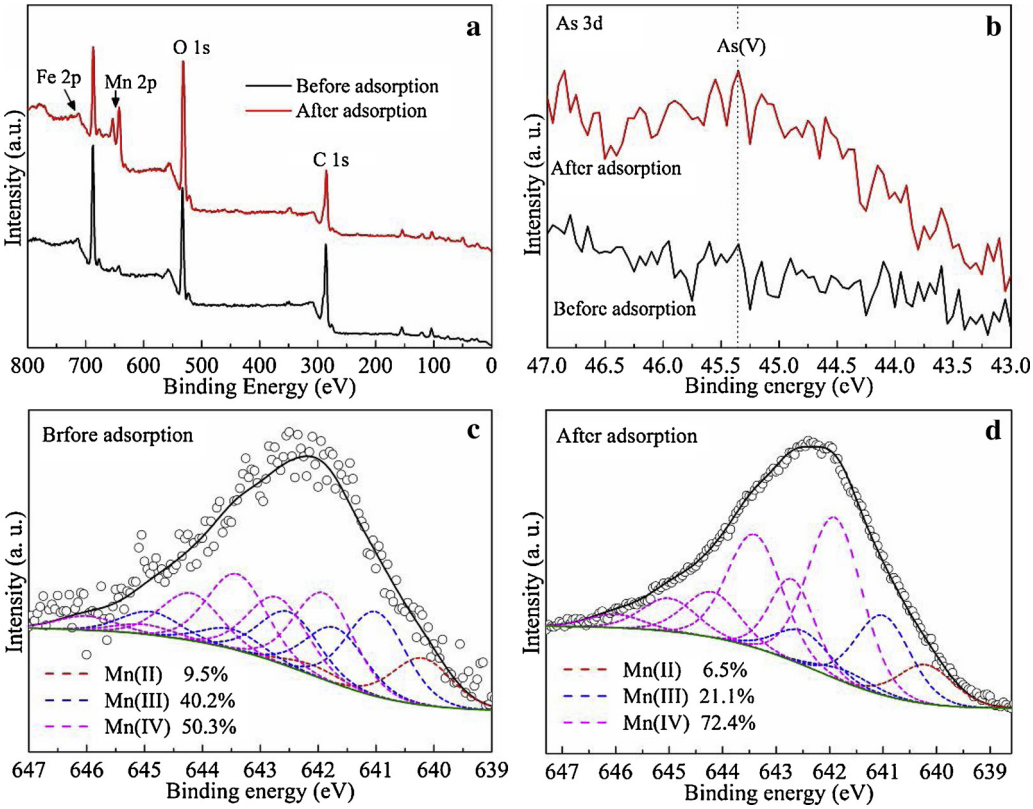

Fig. 9. XPS broad scans (a), Cd 3d (b) and Mn $2p_{3/2}$ (c, d) of ZY before and after electrochemical adsorption at 1.2 V in As-containing wastewater.

facilitates the electrochemical adsorption for Cd(II) (Table S8).

As reported, Mn(II) can be released during the charge-discharge of MnO_2 in acidic electrolyte (Long et al., 2003). In this work, Mn(II) release was also observed in the solution (Fig. S6), resulting in a decrease in the electrochemical adsorption capacity of Cd(II) at low pH. Additionally, the surface charge significantly affects the adsorption capacity of Fe and Mn oxides for heavy metals. The PZC of ZY was determined to be 3.28 (Fig. S18). The surface negative charge of ZY increased with increasing pH from 3.0–6.0, leading to an increase in Cd (II) adsorption capacity at high pH (Spark et al., 1995).

Electrochemical redox reactions changed the chemical composition of Fe-Mn nodule surface and increased the effective adsorption sites for heavy metal ions. The active sites inside the adsorbent cannot be fully utilized, because the adsorption occurs mainly at the bulk electrode/solution interface (Zhou et al., 2018). In our previous work, active adsorption sites were well exposed to heavy metal ions during the dissolution-recrystallization process of birnessite controlled by galvanostatic charge-discharge, achieving superb adsorption capacity for Cd (II), Zn(II) and Cu(II) (Liu et al., 2017a; Peng et al., 2016; Yang et al., 2018). The reduction reaction of birnessite may also help to make full use of the adsorption sites (Manning et al., 2002). More adsorption sites of birnessite were exposed to Cd(II) on the surface of nodules after electrochemical reduction (Figs. 5 and 6), thereby improving the electrochemical adsorption capacity.

4.2. Electrochemical adsorption mechanism for arsenic

Goethite is generally regarded as an excellent adsorbent for As, and its isothermal adsorption capacity for As is significantly higher than that of birnessite (Violante and Pigna, 2002). However, multiple regression analysis showed that birnessite rather than goethite in Fe-Mn nodule plays a major role in the electrochemical adsorption for As (Table S9). The effect of birnessite can also be proved by the increase in the relative contents of Mn and O on the surface of Fe-Mn nodules after electrochemical adsorption of As (Table. S6). Electrochemically controlled redox reactions promote electron/charge transfer in the faradaic process and significantly enhance adsorption capacity (Li et al., 2018). The transformation from Mn(II/III) to Mn(IV) occurs at a higher potential (Hand and Cusick, 2017), which leads to an increase in positive charge on the nodule surface (Fig. 9c–d). Under the action of electric field and diffusion, arsenic would migrate to the Fe-Mn nodule anode and was adsorbed on the surface to balance the increased positive charge. The increase in Mn AOS on the surface after adsorption confirmed this process. The removal efficiency of total As was thus improved due to the electrochemical oxidation of birnessite.

At 1.2 V, the concentrations of As(III) decreased (Fig. 8b), and As(V) was adsorbed on the anode (Fig. 9b). The oxidation of As(III) occurred due to both chemical and electrochemical effects. When As(III,V) is adsorbed on the surface of birnessite, As(V) can be generated from the oxidation of As(III) on the birnessite surface and then released to the solution, and Mn(IV) is reduced to Mn(III) in birnessite (Manning et al., 2002). Adsorption and complexation reactions of As(III) on two Mn(III) reactive sites occur, and two electrons of As(III) are transferred to Mn (III) with the formation of As(V) (Hou et al., 2017; Manning et al., 2002; Zhu et al., 2009). Also, As(III) can be oxidized by H_2O_2 formed from the electrochemical reduction of O_2 on the cathode based on the standard potential of O_2/H_2O_2 (0.029 V, *vs.* SCE) (Kim et al., 2016; Wang et al., 2014). At the voltage from 0.3 to 1.2 V, the potential of the cathode from –0.04 to –0.47 V (*vs.* SCE) contributed to the formation of H_2O_2 and oxidation of As(III) (Fig. S15a) (Liu et al., 2019b). As(V) can be directly adsorbed on birnessite in the forms of bidentate-binuclear, bidentate-mononuclear and monodentate-mononuclear complexes, and the former is the most likely form due to its more stable structure than the latter two (Lafferty et al., 2010, 2011).

Reduction and re-oxidation of birnessite facilitate the adsorption of As (Liu et al., 2019b). The reduction of birnessite by As(III) causes changes in the birnessite surface and generation of new adsorption sites for As(V) and thus contributes to the adsorption of As(V) (Manning

et al., 2002). Mn(II) including the reduction product of birnessite in wastewater was electrodeposited as Mn oxides on the anode surface (Fig. 9c–d and S17a), further driving the adsorption for As(V) (Fig. 9b). The decrease of Mn(II) in wastewater after electrochemical adsorption also confirms this process (Fig. 8a). Fe-Mn nodules with high Mn AOS contain a higher proportion of Mn oxides, which is conducive to the oxidation of As(III). The adsorption of As(V) on anode surface can thereby be facilitated by the reduction of birnessite and re-oxidation of Mn(II). Multiple regression analysis also proved that high Mn AOS facilitated the electrochemical adsorption for As(III,V) (Table S9).

The potential of Fe-Mn nodule anode and the existing form of As in wastewater vary with pH, which would affect the adsorption for As (Spark et al., 1995). The enhancement of As adsorption capacity could be mainly ascribed to the oxidation of Mn(II/III) in Fe-Mn nodules in the presence of electric field. With increasing pH from 5.0–7.0, the oxidation of Mn(II/III) on the surface of Fe-Mn nodules declined due to decreases in the potential of ZY anode (Fig. S15b), which is not conducive to the oxidation and adsorption of As (Fig. 8c). The As(III) mainly exists as H_3AsO_3 at pH 5.0–7.8, and As(V) exists as $H_2AsO_4^-$ at pH 5.0, $H_2AsO_4^-$ and $HAsO_4^{2-}$ at pH 7.0, and $HAsO_4^{2-}$ at pH 7.8 (Song et al., 2017). As for the original wastewater, the initial pH of 7.8 significantly facilitated the ionization of $H_2AsO_4^-$, though the potential of ZY anode showed a slight decrease. The charge of As(V) was remarkably enhanced, promoting the adsorption of As(V) (Fig. 8c). Therefore, the As removal efficiency decreased first and then increased with increasing initial pH.

The adsorption capacity of Fe-Mn nodules for arsenic was significantly higher than that of some natural adsorbents (Table S10). For example, the adsorption capacities of rice straw biochar and polymetallic sea nodule were 0.45 and 0.74 mg g^{-1} for As(III), and 0.55 and 0.74 mg g^{-1} for As(V), respectively. In this work, the adsorption capacity for total As by Fe-Mn nodules at open circuit reached 1.23 mg g^{-1} from industrial wastewater containing 11 % As(III) and 89 % As(V), and was significantly elevated to 1.46 mg g^{-1} by electrochemical oxidation. Therefore, the abundant and eco-friendly Fe-Mn nodules have great potential to be applied to real wastewater treatment.

In this work, the electrochemically driven redox reactions were accompanied by changes in the chemical composition of Fe-Mn nodules and the corresponding adsorption capacity for Cd(II) and As(III,V). The redox reaction and the adsorption mechanism may well explain the enrichment processes of heavy metals in Fe-Mn nodules in natural environments. Fe and Mn oxides in soils have important kinetic effects on the migration of heavy metals, and the concentration of heavy metals in soil solutions is associated with the redox of Fe/Mn oxides (Palumbo et al., 2001). The formation of Fe-Mn nodules in the soils can be attributed to the alternate redox reactions under the conditions of soil wet-dry alternation. Under the condition of waterlogging, Fe(II) and Mn (II) ions are released to soil solutions due to the reduction of Fe and Mn oxides. When the soils are dried, Fe(II) and Mn(II) ions are oxidized and deposited on the surface of Fe and Mn oxides (Liu et al., 2002). Therefore, Fe-Mn nodules are easily enriched with some toxic metals probably due to the redox of Fe and Mn oxides during the formation processes, and the content of heavy metals in the Fe-Mn nodules (*e.g.*, Cd, Ba, Pb, Cr, As) can be 4.3–13.8 times that in the corresponding soil (Gasparatos, 2013; Latrille et al., 2001). Therefore, the electrochemical redox of Fe-Mn nodules contributes much to the adsorption of heavy metals, which may improve the understanding of the enrichment processes of Fe-Mn nodules for heavy metals in natural environments.

5. Conclusions

The chemical composition of natural Fe-Mn nodules was regulated by electrochemical redox reactions to effectively adsorb Cd(II) and As (III,V). The highest electrochemical adsorption capacity for Cd(II) reached 129.9 mg g^{-1}, and the highest electrochemical removal efficiency for total As reached 83.6 %, reducing the total As concentration from 4.068 to 0.669 mg L^{-1}. The adsorption capacity is affected by the chemical composition of Fe-Mn nodules such as birnessite content, voltage and pH. Birnessite in Fe-Mn nodules is the key component for electrochemical adsorption, and the heavy metal cation Cd(II) and anions As(III,V) can be effectively adsorbed under electrochemical reduction and oxidation, respectively. The nodules with high Mn AOS can effectively adsorb Cd(II) and As(III,V) by the electrochemical reduction and oxidation reactions, respectively. Additionally, the reduction of birnessite and electrochemical re-oxidation of Mn(II) in wastewater on the anode surface can contribute to the adsorption of As. The high voltage promotes the redox reactions of birnessite in the Fe-Mn nodules and the adsorption for Cd(II) and As(III,V). The dissolution of Fe-Mn nodules at low pH does not facilitate the adsorption of Cd(II). The oxidation of Mn(II/III) on the surface of Fe-Mn nodule anode declines and the charge of As(V) increases with increasing pH from 5.0–7.8, resulting in a first decrease and then an increase in As removal efficiency. On the basis of this work, the symmetric electrode system with Fe-Mn nodule cathode and anode needs to be further investigated, which may improve the system tested in this study and facilitate the purification of complex real water polluted by different types of heavy metals.

CRediT authorship contribution statement

Qi Qiao: Formal analysis, Writing - original draft, Investigation. **Xiong Yang:** Formal analysis, Writing - review & editing. **Lihu Liu:** Formal analysis, Writing - review & editing. **Yao Luo:** Formal analysis, Writing - Review & Editing. **Wenfeng Tan:** Supervision. **Chengshuai Liu:** Supervision. **Zhi Dang:** Supervision. **Guohong Qiu:** Supervision, Project administration, Conceptualization.

Declaration of Competing Interest

The authors declare that they have no known competing financial interests or personal relationships that could have appeared to influence the work reported in this paper.

Acknowledgements

This work was supported by the National Key Research and Development Program of China (Nos. 2017YFD0801000 and 2018YFD0800304), the National Natural Science Foundation of China (Nos. 41571228, 41425006, 41877025 and 41877528), and the Fundamental Research Funds for the Central Universities (Program Nos. 2662018JC055 and 2662017JC025). We greatly acknowledge Dr. Lirong Zheng and Shengqi Chu at Beijing Synchrotron Radiation Facility and Dr. Lihong Qin at Public Laboratory of Electron Microscope of Huazhong Agricultural University for the data collection and analysis.

Appendix A. Supplementary data

Supplementary material related to this article can be found, in the online version, at doi:https://doi.org/10.1016/j.jhazmat.2020.122165.

References

Boland, D.D., Collins, R.N., Miller, C.J., Glover, C.J., Waite, T.D., 2014. Effect of solution and solid-phase conditions on the Fe(II)-accelerated transformation of ferrihydrite to lepidocrocite and goethite. Environ. Sci. Technol. 48, 5477–5485.

Chakravarty, S., Dureja, V., Bhattacharyya, G., Maity, S., Bhattacharjee, S., 2002. Removal of arsenic from groundwater using low cost ferruginous manganese ore. Water Res. 36, 625–632.

Collins, C.R., Ragnarsdottir, K.V., Sherman, D.M., 1999. Effect of inorganic and organic ligands on the mechanism of cadmium sorption to goethite. Geochim. Cosmochim. Acta 63, 2989–3002.

Deschamps, E., Ciminelli, V.S.T., Höll, W.H., 2005. Removal of As(III) and As(V) from water using a natural Fe and Mn enriched sample. Water Res. 39, 5212–5220.

Feng, X.H., Liu, F., Tan, W.F., Liu, X.W., 2004. Synthesis of birnessite from the oxidation of Mn^{2+} by O_2 in alkali medium: effects of synthesis conditions. Clays Clay Miner. 52, 240–250.
Feng, X.H., Zhai, L.M., Tan, W.F., Liu, F., He, J.Z., 2007. Adsorption and redox reactions of heavy metals on synthesized mn oxide minerals. Environ. Pollut. 147, 366–373.
Gadde, R.R., Laitinen, H.A., 1974. Heavy metal adsorption by hydrous iron and manganese oxides. Anal. Chem. 46, 2022–2026.
Gasparatos, D., 2013. Sequestration of heavy metals from soil with Fe–Mn concretions and nodules. Environ. Chem. Lett. 11, 1–9.
Giménez, J., Martinez, M., de Pablo, J., Rovira, M., Duro, L., 2007. Arsenic sorption onto natural hematite, magnetite, and goethite. J. Hazard. Mater. 141, 575–580.
Guo, H.M., Ren, Y., Liu, Q., Zhao, K., Li, Y., 2013. Enhancement of arsenic adsorption during mineral transformation from siderite to goethite: mechanism and application. Environ. Sci. Technol. 47, 1009–1016.
Hand, S., Cusick, R.D., 2017. Characterizing the impacts of deposition techniques on the performance of MnO_2 cathodes for sodium electrosorption in hybrid capacitive deionization. Environ. Sci. Technol. 51, 12027–12034.
Hou, J.T., Xiang, Y.J., Zheng, D., Li, Y.Z., Xue, S.G., Wu, C., Hartley, W., Tan, W.F., 2017. Morphology-dependent enhancement of arsenite oxidation to arsenate on birnessite-type manganese oxide. Chem. Eng. J. 327, 235–243.
Kim, J.G., Dixon, J.B., Chusuei, C.C., Deng, Y.J., 2002. Oxidation of chromium (III) to (VI) by manganese oxides. Soil Sci. Soc. Am. J. 66, 306–315.
Kim, T., Yu, J., Kim, C., Yoon, J., 2016. Hydrogen peroxide generation in flow-mode capacitive deionization. J. Electroanal. Chem. 776, 101–104.
Kosmulski, M., 2009. Compilation of PZC and IEP of sparingly soluble metal oxides and hydroxides from literature. Adv. Colloid Interface Sci. 152, 14–25.
Lafferty, B.J., Ginder-Vogel, M., Zhu, M.Q., Livi, K.J.T., Sparks, D.L., 2010. Arsenite oxidation by a poorly crystalline manganese-oxide. 2. Results from X-ray absorption spectroscopy and X-ray diffraction. Environ. Sci. Technol. 44, 8467–8472.
Lafferty, B.J., Ginder-Vogel, M., Sparks, D.L., 2011. Arsenite oxidation by a poorly-crystalline manganese oxide. 3. Arsenic and manganese desorption. Environ. Sci. Technol. 45, 9218–9223.
Lanson, B., Drits, V.A., Silvester, E., Manceau, A., 2000. Structure of H-exchanged hexagonal birnessite and its mechanism of formation from Na-rich monoclinic buserite at low pH. Am. Mineral. 85, 826–838.
Latrille, C., Elsass, F., van Oort, F., Denaix, L., 2001. Physical speciation of trace metals in Fe–Mn concretions from a rendzic lithosol developed on Sinemurian limestones (France). Geoderma 100, 127–146.
Lee, B., Yoon, C.S., Lee, H.R., Chung, K.Y., Cho, B.W., Oh, S.H., 2014a. Electrochemically-induced reversible transition from the tunneled to layered polymorphs of manganese dioxide. Sci. Rep. 4, 6066.
Lee, J., Kim, S., Kim, C., Yoon, J., 2014b. Hybrid capacitive deionization to enhance the desalination performance of capacitive techniques. Energy Environ. Sci. 7, 3683–3689.
Lefkowitz, J.P., Elzinga, E.J., 2015. Impacts of aqueous Mn (II) on the sorption of Zn (II) by hexagonal birnessite. Environ. Sci. Technol. 49, 4886–4893.
Lefkowitz, J.P., Elzinga, E.J., 2017. Structural alteration of hexagonal birnessite by aqueous Mn(II): impacts on Ni(II) sorption. Chem. Geol. 466, 524–532.
Li, P.J., Gui, Y., Blackwood, D.J., 2018. Development of a nanostructured α-MnO_2/carbon paper composite for removal of Ni^{2+}/Mn^{2+} ions by electrosorption. ACS Appl. Mater. Interfaces 10, 19615–19625.
Ling, F.T., Post, J.E., Heaney, P.J., Kubicki, J.D., Santelli, C.M., 2017. Fourier-transform infrared spectroscopy (FTIR) analysis of triclinic and hexagonal birnessites. Spectrochim. Acta, Part A 178, 32–46.
Liu, F., Colombo, C., Adamo, P., He, J.Z., Violante, A., 2002. Trace elements in manganese-iron nodules from a Chinese Alfisol. Soil Sci. Soc. Am. J. 66, 661–670.
Liu, Y.H., Hsi, H.C., Li, K.C., Hou, C.H., 2016. Electrodeposited manganese dioxide/activated carbon composite as a high-performance electrode material for capacitive deionization. ACS Sustain. Chem. Eng. 4, 4762–4770.
Liu, L.H., Luo, Y., Tan, W.F., Liu, F., Suib, S.L., Zhang, Y.S., Qiu, G.H., 2017a. Zinc removal from aqueous solution using a deionization pseudocapacitor with a high-performance nanostructured birnessite electrode. Environ. Sci. Nano 4, 811–823.
Liu, L.H., Qiu, G.H., Suib, S.L., Liu, F., Zheng, L.R., Tan, W.F., Qin, L.H., 2017b. Enhancement of Zn^{2+} and Ni^{2+} removal performance using a deionization pseudocapacitor with nanostructured birnessite and its carbon nanotube composite electrodes. Chem. Eng. J. 328, 464–473.
Liu, L.H., Peng, Q.C., Qiu, G.H., Zhu, J., Tan, W.F., Liu, C.S., Zheng, L.R., Dang, Z., 2019a. Cd^{2+} adsorption performance of tunnel-structured manganese oxides driven by electrochemically controlled redox. Environ. Pollut. 244, 783–791.
Liu, L.H., Tan, W.F., Suib, S.L., Qiu, G.H., Zheng, L.R., Su, S.M., 2019b. Enhanced adsorption removal of arsenic from mining wastewater using birnessite under electrochemical redox reactions. Chem. Eng. J. 375, 122051.
Long, J.W., Rhodes, C.P., Young, A.L., Rolison, D.R., 2003. Ultrathin, protective coatings of poly(*o*-phenylenediamine) as electrochemical proton gates: making mesoporous MnO_2 nanoarchitectures stable in acid electrolytes. Nano Lett. 3, 1155–1161.
Lu, H.B., Zhang, W.F., Tao, L., Liu, F., Zhang, J., 2019. Enhanced removal of antimony by acid birnessite with doped iron ions: companied by the structural transformation. Chemosphere 226, 834–840.
Maity, S., Chakravarty, S., Bhattacharjee, S., Roy, B.C., 2005. A study on arsenic adsorption on polymetallic sea nodule in aqueous medium. Water Res. 39, 2579–2590.
Manning, B.A., Fendorf, S.E., Bostick, B., Suarez, D.L., 2002. Arsenic(III) oxidation and arsenic(V) adsorption reactions on synthetic birnessite. Environ. Sci. Technol. 36, 976–981.
Marcus, M.A., Manceau, A., Kersten, M., 2004. Mn, Fe, Zn and As speciation in a fast-growing ferromanganese marine nodule. Geochim. Cosmochim. Acta 68, 3125–3136.
Nesbitt, H.W., Canning, G.W., Bancroft, G.M., 1998. XPS study of reductive dissolution of 7Å-birnessite by H_3AsO_3, with constraints on reaction mechanism. Geochim. Cosmochim. Acta 62, 2097–2110.
Pai, C.W., Wang, M.K., Wang, W.M., Houng, K.H., 1999. Smectites in iron-rich calcareous soil and black soils of Taiwan. Clays Clay Miner. 47, 389–398.
Palumbo, B., Bellanca, A., Neri, R., Roe, M.J., 2001. Trace metal partitioning in Fe–Mn nodules from Sicilian soils. Italy. Chem. Geol. 173, 257–269.
Peng, Q.C., Liu, L.H., Luo, Y., Zhang, Y.S., Tan, W.F., Liu, F., Suib, S.L., Qiu, G.H., 2016. Cadmium removal from aqueous solution by a deionization supercapacitor with a birnessite electrode. ACS Appl. Mater. Interfaces 8, 34405–34413.
Peng, X., Xi, B.D., Zhao, Y., Shi, Q.T., Meng, X.G., Mao, X.H., Jiang, Y.H., Ma, Z.F., Tan, W.B., Liu, H.L., Gong, B., 2017. Effect of arsenic on the formation and adsorption property of ferric hydroxide precipitates in ZVI treatment. Environ. Sci. Technol. 51, 10100–10108.
Robinson, G.W., 1922. A new method for the mechanical analysis of soils and other dispersions. J. Agric. Sci. 12, 306–321.
Sandroni, V., Smith, C.M., Donovan, A., 2003. Microwave digestion of sediment, soils and urban particulate matter for trace metal analysis. Talanta 60, 715–723.
Singh, M., Sarkar, B., Biswas, B., Churchman, J., Bolan, N.S., 2016. Adsorption-desorption behavior of dissolved organic carbon by soil clay fractions of varying mineralogy. Geoderma 280, 47–56.
Song, P.P., Yang, Z.H., Zeng, G.M., Yang, X., Xu, H.Y., Wang, L.K., Xu, R., Xiong, W.P., Ahmad, K., 2017. Electrocoagulation treatment of arsenic in wastewaters: a comprehensive review. Chem. Eng. J. 317, 707–725.
Spark, K.M., Johnson, B.B., Wells, J.D., 1995. Characterizing heavy-metal adsorption on oxides and oxyhydroxides. Eur. J. Soil Sci. 46, 621–631.
Srodon, J., 2006. Identification and quantitative analysis of clay minerals. In: Bergaya, F., Theng, B.K.G., Lagaly, G. (Eds.), Handbook of Clay Science. Elsevier, Amsterdam, pp. 765–787.
Tan, W.F., Liu, F., Feng, X.H., Huang, Q.Y., Li, X.Y., 2005. Adsorption and redox reactions of heavy metals on Fe–Mn nodules from Chinese soils. J. Colloid Interface Sci. 284, 600–605.
Tan, W.F., Liu, F., Li, Y.H., Hu, H.Q., Huang, Q.Y., 2006. Elemental composition and geochemical characteristics of iron-manganese nodules in main soils of China. Pedosphere 16, 72–81.
Tokashiki, Y., Hentona, T., Shimo, M., Arachchi, L.P., 2003. Improvement of the successive selective dissolution procedure for the separation of birnessite, lithiophorite, and goethite in soil manganese nodules. Soil Sci. Soc. Am. J. 67, 837–843.
Violante, A., Pigna, M., 2002. Competitive sorption of arsenate and phosphate on different clay minerals and soils. Soil Sci. Soc. Am. J. 66, 1788–1796.
Wang, Y., Feng, X.H., Villalobos, M., Tan, W.F., Liu, F., 2012. Sorption behavior of heavy metals on birnessite: relationship with its Mn average oxidation state and implications for types of sorption sites. Chem. Geol. 292, 25–34.
Wang, X.Q., Liu, C.P., Yuan, Y., Li, F.B., 2014. Arsenite oxidation and removal driven by a bio-electro-Fenton process under neutral pH conditions. J. Hazard. Mater. 275, 200–209.
Wu, Y., Kukkadapu, R.K., Livi, K.J., Xu, W.Q., Li, W., Sparks, D.L., 2018. Iron and arsenic speciation during As(III) oxidation by manganese oxides in the presence of Fe(II): molecular-level characterization using XAFS, Mössbauer, and TEM analysis. ACS Earth Space Chem. 2, 256–268.
Xu, P., Zeng, G.M., Huang, D.L., Feng, C.L., Hu, S., Zhao, M.H., Lai, C., Wei, Z., Huang, C., Xie, G.X., Liu, Z.F., 2012. Use of iron oxide nanomaterials in wastewater treatment: a review. Sci. Total Environ. 424, 1–10.
Xu, J., Li, J.J., Wu, F., Zhang, Y., 2013. Rapid photooxidation of As(III) through surface complexation with nascent colloidal ferric hydroxide. Environ. Sci. Technol. 48, 272–278.
Yang, D.S., Wang, M.K., 2003. Characterization and a fast method for synthesis of submicron lithiophorite. Clays Clay Miner. 51, 96–101.
Yang, X., Liu, L.H., Tan, W.F., Qiu, G.H., Liu, F., 2018. High-performance Cu^{2+} adsorption of birnessite using electrochemically controlled redox reactions. J. Hazard. Mater. 354, 107–115.
Yang, S.T., Uesugi, S., Qin, H.B., Tanaka, M., Kurisu, M., Miyamoto, C., Kashiwabara, T., Usui, A., Takahashi, Y., 2019a. Comparison of arsenate and molybdate speciation in hydrogenetic ferromanganese nodules. ACS Earth Space Chem. 3, 29–38.
Yang, X., Liu, L.H., Zhang, M.Z., Tan, W.F., Qiu, G.H., Zheng, L.R., 2019b. Improved removal capacity of magnetite for Cr(VI) by electrochemical reduction. J. Hazard. Mater. 374, 26–34.
Zhang, S.W., Chen, G.Z., 2008. Manganese oxide based materials for supercapacitors. Energy Mater. 3, 186–200.
Zhang, G.S., Qu, J.H., Liu, H.J., Liu, R.P., Li, G.T., 2007. Removal mechanism of As (III) by a novel Fe－Mn binary oxide adsorbent: oxidation and sorption. Environ. Sci. Technol. 41, 4613–4619.
Zhang, C.Y., He, D., Ma, J.X., Tang, W.W., Waite, T.D., 2018. Faradaic reactions in capacitive deionization (CDI)-problems and possibilities: a review. Water Res. 128, 314–330.
Zhao, H.Y., Zhu, M.Q., Li, W., Elzinga, E.J., Villalobos, M., Liu, F., Zhang, J., Feng, X.H., Sparks, D.L., 2016. Redox reactions between Mn(II) and hexagonal birnessite change its layer symmetry. Environ. Sci. Technol. 50, 1750–1758.
Zhou, Y.J., Ji, Q.H., Liu, H.J., Qu, J.H., 2018. Pore structure-dependent mass transport in flow-through electrodes for water remediation. Environ. Sci. Technol. 52, 7477–7485.
Zhu, M.Q., Paul, K.W., Kubicki, J.D., Sparks, D.L., 2009. Quantum chemical study of arsenic (III, V) adsorption on Mn-oxides: implications for arsenic(III) oxidation. Environ. Sci. Technol. 43, 6655–6661.